Available online at www.sciencedirect.com
ScienceDirect
International Journal of Heat and Mass Transfer 51 (2008) 4353–4366
International Journal of HEAT and MASS TRANSFER
www.elsevier.com/locate/ijhmt

Modeling of transport phenomena in hybrid laser-MIG keyhole welding

J. Zhou [a,*], H.L. Tsai [b]

[a] Department of Mechanical Engineering, Pennsylvania State University Erie, Erie, PA 16563, USA
[b] Department of Mechanical and Aerospace Engineering, University of Missouri-Rolla, 1870 Miner Circle, Rolla, MO 65409-1350, USA

Received 13 June 2007; received in revised form 13 February 2008
Available online 25 April 2008

Abstract

Mathematical models and associated numerical techniques have been developed to investigate the complicated transport phenomena in spot hybrid laser-MIG keyhole welding. A continuum formulation is used to handle solid phase, liquid phase, and the mushy zone during the melting and solidification processes. The volume of fluid (VOF) method is employed to handle free surfaces, and the enthalpy method is used for latent heat. Dynamics of weld pool fluid flow, energy transfer in keyhole plasma and weld pool, and interactions between droplets and weld pool are calculated as a function of time. The effect of droplet size on mixing and solidification is investigated. It is found that weld pool dynamics, cooling rate, and final weld bead geometry are strongly affected by the impingement process of the droplets in hybrid laser-MIG welding. Also, compositional homogeneity of the weld pool is determined by the competition between the rate of mixing and the rate of solidification.

Keywords: Hybrid laser-MIG welding; Keyhole; Mixing; Diffusion; Mathematical model

1. Introduction

Laser keyhole welding is widely used in the auto and shipbuilding industries due to its high precision, deep-penetration depths, low heat input, small weldment distortion and high welding speed [1–4]. However, in laser keyhole welding, pores/voids are frequently observed, especially in laser welding of certain alloys, such as 5000 and 6000 series aluminum alloys, which are desired for their excellent corrosion resistance and substantial strength [5]. The low melting-point elements in the alloys, such as aluminum or magnesium, are easily vaporized and lost from the weld region, leading to the formation of porosity, cracking susceptibility, changes of composition and mechanical properties, and other defects [6–8]. In addition, serious hot cracks caused by large cooling rates are also commonly found in laser welding of aluminum alloys.

Hybrid laser-metal inert gas (MIG) welding, by combining laser welding and arc welding, can offer many advantages over laser welding or arc welding alone. Some advantages are elimination of undercut, prevention of porosity formation, and modification of weld compositions [9–14]. In hybrid welding, compositions of base metal and filler metal are usually different. By adding some anti-crack elements through the filler droplets, the aforementioned problems in laser welding, such as hot-cracking susceptibility, strength reduction, etc. can be reduced or eliminated. Missouri and Sili [15] reported that adding filler metal could offer advantages in the chemical composition of the weld zone, which could have a positive effect on the impact toughness and on the resistance to porosity for laser welding of high-strength structural steels. Hwang et al. [16] suggested that the added wire filler material had positive effects on the fatigue properties of SPCC-CQ1 cold rolled steel. Schubert et al. [17] proposed that formation of hot cracks in aluminum welding was determined by the temperature–time-cycle, mixing, and chemical compositions in regions of high crack sensitivities. Also, with additional heat and

* Corresponding author. Tel.: +1 912 225 0587; fax: +1 814 898 6125.
E-mail address: jzhou@georgiasouthern.edu (J. Zhou).

0017-9310/$ - see front matter © 2008 Elsevier Ltd. All rights reserved.
doi:10.1016/j.ijheatmasstransfer.2008.02.011

Nomenclature

A	constant in Eq. (12)
A_v	constant in Eq. (16)
B_0	constant in Eq. (12)
c_p	specific heat of metal
c_{pl}	specific heat of plasma
c	the speed of light
C	coefficient in Eqs. (2) and (3)
e	charge of electron
E_i	ionization potential for neutral atom
f^α	species (sulfur) concentration
F	volume of fluid function
g	gravitational acceleration
g_e	degeneracy factor of electron particle
g_i	degeneracy factor of ion particle
g_0	degeneracy factor of neutral atom
$\bar{g}$	quantum mechanical Gaunt factor
h	enthalpy for metal
h_{pl}	enthalpy for plasma
h_{conv}	convective heat transfer coefficient
$\bar{h}$	Planck's constant
H_v	latent heat for liquid–vapor
H_b	thickness of base metal
$I(\boldsymbol{r}, \boldsymbol{s})$	total directional radiative intensity
I_b	black body emission intensity
$I_c(r)$	collimate incident laser beam intensity distribution on the focus plane
$I_o(r,z)$	incident intensity from laser beam
$I_{r,m}(r,z)$	incident intensity from mth reflection
k_a	Planck mean absorption coefficient
k_b	Boltzmann constant
k_{pl}	thermal conductivity of plasma
k	thermal conductivity of metal
K	permeability function in Eqs. (2) and (3)
K_{pl}	Inverse Bremsstrahlung (IB) absorption coefficient
m_a	atomic mass
m_e	electron mass
m_v	variable defined in Eq. (43)
m	times of reflection
M_K	Mach number at the outer of the Knudsen layer
$\vec{n}$	vector normal to local free surface
n_e	electron density in plasma
n_i	ion density in plasma
n_0	neutral particle density in plasma
N_a	Avogadro's number
p	pressure in liquid metal
P_{laser}	laser power
P_r	recoil pressure
P_σ	surface tension
q_{conv}	heat loss by convection
q_{evap}	heat loss by evaporation
q_{laser}	heat flux by laser irradiation
q_{rad}	heat loss by radiation
$\boldsymbol{q}_r$	radiation heat flux vector
r-z	cylindrical coordinate system
r_f	laser beam radius
r_{fo}	laser beam radius at the focal position
R	gas constant
R_b	radius of base metal
$\vec{s}$	vector tangential to local free surface
t	time
T	temperature of metal
T_0	reference temperature
T_K	plasma temperature outside of Knudsen layer
T_{pl}	temperature of plasma
$\overline{T_{pl}}$	average plasma temperature
T_w	surface temperature of the liquid metal at the keyhole wall
T_∞	ambient temperature
u	velocity in r-direction
U	variable defined in Eq. (13)
v	velocity in z-direction
$\boldsymbol{V}$	velocity vector
$\boldsymbol{V}_r$	relative velocity vector ($\boldsymbol{V}_l$–$\boldsymbol{V}_s$)
W	melt mass evaporation rate
Z	charge of ion

Greek symbols

α_{Fr}	Fresnel absorption coefficient
β_T	thermal expansion coefficient
$\partial\gamma/\partial T$	surface tension temperature gradient
$\partial\gamma/\partial f^\alpha$	surface tension concentration gradient
ε	surface radiation emissivity
ε_0	dielectric constant
ε_f	constant in Eq. (18)
γ	surface tension coefficient
γ_r	specific heat ratio
ω	angular frequency of laser irradiation
Ω	solid angle
κ	free surface curvature
μ_l	dynamic viscosity
σ	Stefan–Boltzmann constant
σ_e	electrical conductivity
φ	angle of incident laser light
ρ	density of metal
ρ_{pl}	density of plasma
$\tau_{\vec{s}}$	Marangoni shear stress

Subscripts

0	initial value
c	original incident laser light
l	liquid phase
r	relative to solid velocity
(r,m)	mth reflected laser beam
pl	plasma
s	solid phase

mass inputs from the arc and the filler droplets in hybrid laser-MIG welding, deep-penetration hybrid welds without voids/pores can be achieved.

So far, most of the hybrid laser-MIG welding research is concentrating on how to effectively combine a laser welding process with an arc welding process together by experimental methods [9,10,17–19]. There is very limited research focusing on the study of the complicated transport phenomena, such as melt flow, heat transfer, and especially mixing phenomenon, which are involved in hybrid laser-MIG welding. However, understanding these transport phenomena is critical for fundamentally understanding and optimizing the hybrid laser-MIG welding process. For example, in order to achieve good anti-crack characteristics of an aluminum weld by adding filler metal in laser-MIG welding, it is necessary to understand how well the droplets can mix and diffuse into the weld pool and how fast the weld pool solidifies.

In this study, mathematical models have been developed to investigate transport phenomena in hybrid laser-MIG welding. The laser keyhole welding models developed by Zhou et al. [20] are modified to simulate the spot hybrid laser-MIG keyhole welding process. It includes calculations of the temperature field, pressure balance, melt flow, free surface evolution, laser-induced plasma formation, and multiple reflections in a typical hybrid laser-MIG welding process. The transient energy transport in the weld pool and the keyhole plasma, interactions between droplets and the weld pool, weld pool dynamics, and the effects of filler droplets on the final weld bead profiles as well as composition distributions in the weld pool are all systematically investigated.

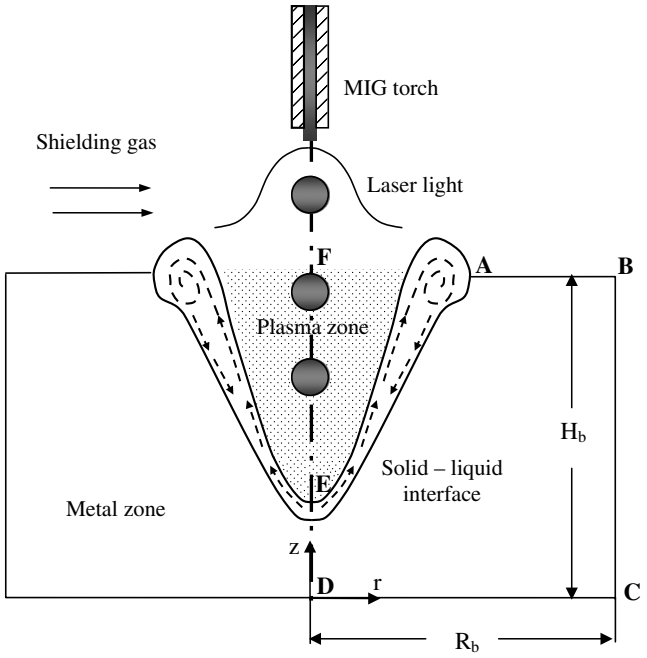

Fig. 1. Schematic sketch of a spot hybrid laser-MIG welding process.

2. Mathematical model

Fig. 1 shows a schematic sketch of the spot hybrid laser-MIG welding process. A control volume method employing the volume of fluid (VOF) technique [21] and the continuum formulation [22] is used to calculate the momentum and energy transport in the weld pool. The VOF technique can handle a transient deformed weld pool surface, while the continuum formulation can handle fusion and solidification of the liquid region, the mush zone and the solid region. Plasma in the keyhole is treated as the vapor of weld material. Although the velocity and pressure change dramatically across the Knudsen layer, the generic translation vapor flow along the keyhole is neglected [23] and, in the present study, only the temperature distribution is considered. Meanwhile, the pressure along the keyhole is considered to be approximately constant [24] and is comparable to the atmospheric pressure. Note in high power laser welding ($\geqslant 8$ kW), the plasma plume and its velocities in the keyhole can be very significant [4], hence, the assumption of no plasma flow in the present study is limited to low power laser keyhole welding.

2.1. Metal zone simulation

2.1.1. Governing equations

The governing differential equations used to describe the heat and mass transfer and fluid flow in a cylindrical coordinate (r-z) system given by Chiang and Tsai [22] are modified and used in the present study:

Continuity

$$\frac{\partial}{\partial t}(\rho) + \nabla \cdot (\rho V) = 0 \tag{1}$$

Momentum

$$\frac{\partial}{\partial t}(\rho u) + \nabla \cdot (\rho V u) = \nabla \cdot \left(\mu_l \frac{\rho}{\rho_l} \nabla u\right) - \frac{\partial p}{\partial r} - \frac{u_l}{K}\frac{\rho}{\rho_l}(u - u_s) - \frac{C\rho^2}{K^{0.5}\rho_l}|u - u_s|(u - u_s) - \nabla \cdot (\rho f_s f_l V_r u_r) + \nabla \cdot \left(\mu_s u \nabla\left(\frac{\rho}{\rho_l}\right)\right) \tag{2}$$

$$\frac{\partial}{\partial t}(\rho v) + \nabla \cdot (\rho V v) = \rho g + \nabla \cdot \left(\mu_l \frac{\rho}{\rho_l} \nabla v\right) - \frac{\partial p}{\partial z} - \frac{u_l}{K}\frac{\rho}{\rho_l}(v - v_s) - \frac{C\rho^2}{K^{0.5}\rho_l}|v - v_s|(v - v_s) - \nabla \cdot (\rho f_s f_l V_r v_r) + \nabla \cdot \left(\mu_s v \nabla\left(\frac{\rho}{\rho_l}\right)\right) + \rho g \beta_T (T - T_0) \tag{3}$$

Energy

$$\frac{\partial}{\partial t}(\rho h)+\nabla\cdot(\rho \boldsymbol{V} h)=\nabla\cdot\left(\frac{k}{c_p}\nabla h\right)-\nabla\cdot\left(\frac{k}{c_p}\nabla(h_s-h)\right)-\nabla\cdot(\rho(\boldsymbol{V}-\boldsymbol{V}_s)(h_l-h)) \quad (4)$$

Species

$$\frac{\partial}{\partial t}(\rho f^{\alpha})+\nabla\cdot(\rho \boldsymbol{V} f^{\alpha})=\nabla\cdot(\rho D\nabla f^{\alpha})-\nabla\cdot(\rho D\nabla(f_l^{\alpha}-f^{\alpha}))-\nabla\cdot(\rho(\boldsymbol{V}-\boldsymbol{V}_s)(f_l^{\alpha}-f^{\alpha})) \quad (5)$$

The physical meaning of each term appearing in the above equations can be found in Ref. [22]. In Eqs. (1)–(5), the continuum density, specific heat, thermal conductivity, solid mass fraction, liquid mass fraction, mass diffusivity, velocity and enthalpy are defined in Ref. [25].

2.2. Tracking of free surfaces

The algorithm of VOF is used to track the dynamics of free surfaces. The fluid configuration is defined by a volume of fluid function, $F(r, z, t)$, which tracks the location of free surface. The function F takes the value of one for the cell full of fluid and the value of zero for the empty cell. Cells with F values between zero and one are partially filled with fluid and identified as surface cells. The function F is governed by the following equation:

$$\frac{dF}{dt}=\frac{\partial F}{\partial t}+(\boldsymbol{V}\cdot\nabla)F=0 \quad (6)$$

2.3. Boundary conditions

The boundaries of the metal zone simulation are divided into five segments, as shown in Fig. 1.

2.3.1. Top surface inside the keyhole (AE in Fig. 1)

For cells containing free surface, that is, cells that contain fluid but have one or more empty neighbors, in the direction normal to the free surface, the following pressure condition must be satisfied [1]:

$$P=P_{\sigma}+P_r \quad (7)$$

where P is the pressure at the free surface in a direction normal to the local free surface. P_{σ} is the surface tension and P_r is the recoil pressure. P_{σ} is calculated by the following formula:

$$P_{\sigma}=\kappa\gamma \quad (8)$$

where κ is the free surface curvature, given by [25]:

$$\kappa=-\left[\nabla\cdot\left(\frac{\vec{n}}{|\vec{n}|}\right)\right]=\frac{1}{|\vec{n}|}\left[\left(\frac{\vec{n}}{|\vec{n}|}\cdot\nabla\right)|\vec{n}|-(\nabla\cdot\vec{n})\right] \quad (9)$$

where $\vec{n}$ is the unit vector normal to the local free surface. For a pseudo-binary Fe–S system, the surface tension coefficient γ can be calculated as a function of temperature T and sulfur concentration f^{α} [26]

$$\gamma=1.943-4.3\times10^{-4}(T-1723)-RT\times1.3\times10^{-8}\times\ln\left[1+0.00318f^{\alpha}\exp\left(\frac{1.66\times10^{8}}{RT}\right)\right] \quad (10)$$

In this study, the temperature and concentration dependent Marangoni shear stress on the free surface in the direction tangential to the local surface is given by [27]:

$$\tau_{\vec{s}}=\mu_l\frac{\partial(\boldsymbol{V}\cdot\vec{s})}{\partial\vec{n}}=\frac{\partial\gamma}{\partial T}\frac{\partial T}{\partial\vec{s}}+\frac{\partial\gamma}{\partial f^{\alpha}}\frac{\partial f^{\alpha}}{\partial\vec{s}} \quad (11)$$

Calculation of the evaporation-induced recoil pressure P_r is complicated by the existence of a Knudsen layer over the vaporizing surface. Based on Knight's model [28], the recoil pressure can be calculated by [29]:

$$P_r=AB_0/\sqrt{T_w}\exp(-U/T_w) \quad (12)$$

where A is the numerical coefficient and B_0 is the vaporization constant. The coefficient A depends on the ambient pressure and its value varies from 0.55 for evaporation in the vacuum to 1 for the case of evaporation under a high ambient pressure. For atmospheric pressure, the coefficient A is close to its minimal value of 0.55. B_0 is at the value of 1.78×10^{10}. T_w is the surface temperature of the liquid metal on the keyhole wall. The parameter U is defined as follows [29]:

$$U=m_aH_v/(N_ak_b) \quad (13)$$

where m_a is atomic mass, H_v is the latent heat of evaporation, N_a is the Avogadro's number and k_b is the Boltzmann constant.

The energy on the top free surface is balanced between the laser irradiation, plasma-keyhole wall radiation, the heat dissipation through convection, and metal vaporization. In general, since the velocity of the plume along the surface is assumed to be zero [23], the heat loss due to convection is omitted. The energy balance is given by the following formula:

$$k\frac{\partial T}{\partial\vec{n}}=q_{laser}+q_{rad}-q_{evap} \quad (14)$$

In this study, the liquid/vapor evaporation model is used due to the low intensity of laser irradiation. The heat loss due to surface evaporation can be written as [30]

$$q_{evap}=WH_v \quad (15)$$

$$\log(W)=A_v+\left(6.121-\frac{18836}{T}\right)-0.5\log T \quad (16)$$

The laser heat flux q_{laser} comes from the Fresnel absorption of the incident intensity directly from the laser beam plus the incident intensity from the multiple reflections:

$$q_{\text{laser}} = I_{\text{o}}(r,z)\alpha_{\text{Fr}}(\varphi_{\text{o}}) + \sum_{m=1}^{n} I_{r,m}(r,z)\alpha_{\text{Fr}}(\varphi_m) \tag{17}$$

$$\alpha_{\text{Fr}}(\varphi) = 1 - \frac{1}{2}\left(\frac{1+(1-\varepsilon_{\text{f}}\cos\varphi)^2}{1+(1+\varepsilon_{\text{f}}\cos\varphi)^2} + \frac{\varepsilon_{\text{f}}^2 - 2\varepsilon_{\text{f}}\cos\varphi + 2\cos^2\varphi}{\varepsilon_{\text{f}}^2 + 2\varepsilon_{\text{f}}\cos\varphi + 2\cos^2\varphi}\right) \tag{18}$$

where φ is the angle of the incident light with the normal of the keyhole surface, n is the total number of incident light from multiple reflections. ε_{f} is a material-dependent coefficient. In CO_2 laser welding of mild steel, $\varepsilon_{\text{f}} = 0.2$ is used. $I_{\text{o}}(r,z)$ and $I_{\text{r},m}(r,z)$ are, respectively, the incident intensity from laser beam and the mth multiple reflection at the keyhole wall which are given as

$$I_{\text{o}}(r,z) = I_{\text{c}}(r)\exp\left(-\int_0^{z_0} K_{\text{pl}}\mathrm{d}z\right) \tag{19}$$

$$I_{r,m}(r,z) = I_{\text{r}}(r,z)\exp\left(-\int_0^{z_m} K_{\text{pl}}\mathrm{d}z\right) \tag{20}$$

$$I_{\text{r}}(r,z) = I_{\text{o}}(r,z)(1-\alpha_{\text{Fr}}) \tag{21}$$

where $I_{\text{c}}(r)$ stands for the original collimated incident laser beam intensity, $I_{r,m}(r, z)$ is the reflected laser beam intensity at the m times reflections, $\int_0^{z_0} K_{\text{pl}}\mathrm{d}z$ and $\int_0^{z_m} K_{\text{pl}}\mathrm{d}z$ are the optical thickness of the laser transportation path, respectively, for the first incident and the multiple reflections, and K_{pl} is the plasma absorption coefficient due to the Inverse Bremsstrahlung (IB) absorption [31]

$$K_{\text{pl}} = \frac{n_{\text{e}} n_{\text{i}} Z^2 e^6 2\pi}{6\sqrt{3} m \varepsilon_0^3 c \bar{h} \omega^3 m_{\text{e}}^2}\left(\frac{m_{\text{e}}}{2\pi k_{\text{b}} T_{\text{pl}}}\right)^{0.5}\left[1-\exp\left(-\frac{\omega}{k_{\text{b}}T_{\text{pl}}}\right)\right]\bar{g} \tag{22}$$

where Z is the charge of ion in the plasma, e is the charge of electron, ω is the angular frequency of the laser irradiation, ε_0 is the dielectric constant, n_{e} and n_{i} are the densities of electrons and ions respectively, $\bar{h}$ is the Planck's constant, m is a constant that is related to the specific laser being used and is one for CO_2 laser, m_{e} is the electron mass, T_{pl} is the plasma temperature, c is the speed of light, and $\bar{g}$ is the quantum mechanical Gaunt factor. For weakly ionized plasma in the keyhole, Saha equation [32] can be used to calculate the densities of the plasma species

$$\frac{n_{\text{e}} n_{\text{i}}}{n_0} = \frac{g_{\text{e}} g_{\text{i}}}{g_0}\frac{(2\pi m_{\text{e}} k_{\text{b}} T_{\text{pl}})^{1.5}}{\bar{h}^3}\exp\left(-\frac{E_{\text{i}}}{k_{\text{b}}T_{\text{pl}}}\right) \tag{23}$$

where n_0 is neutral particle density which is $10^{26}/\text{cm}^3$ for iron [32], g_{e}, g_{i} and g_0 are, respectively, the degeneracy factors for electrons, ions and neutral atoms, E_{i} is the ionization potential for the neutral atoms in the gas. Assuming the laser intensity distribution is ideal Gaussian-like, $I_{\text{c}}(r)$ can be written as [33]

$$I_{\text{c}}(r) = \frac{2P_{\text{laser}}}{\pi r_{\text{fo}}^2}\left(\frac{r_{\text{f}}}{r_{\text{fo}}}\right)^2\exp\left(-\frac{2r^2}{r_{\text{f}}^2}\right) \tag{24}$$

where r_{f} is the beam radius, r_{fo} is the beam radius at the focal position, and P_{laser} is the laser power. In laser welding, the keyhole surface temperature is much lower than that of the plasma, so the radiation and emission of the surface can be omitted. Then q_{rad} can be simplified as

$$q_{\text{rad}} = \varepsilon\sigma(\overline{T_{\text{pl}}}^4 - T^4) \tag{25}$$

where $\overline{T_{\text{pl}}}$ is the average temperature of keyhole plasma.

2.3.2. Top surface outside the keyhole (AB in Fig. 1)

Boundary condition on the top surface outside the keyhole is similar to that inside the keyhole. The differences lie in the absence of plasma and multiple reflections. As shown in Fig. 1, there is a shielding gas flow above the base metal, which means that plasma outside the keyhole will be blown away. So Eq. (17) can be written as

$$q_{\text{laser}} = I_{\text{o}}(r,z)\alpha_{\text{Fr}}\cos\varphi \tag{26}$$

Since there is no plasma and the temperature of shielding gas is much lower than that of the metal surface, the radiation heat flux can be given as

$$q_{\text{rad}} = -\varepsilon\sigma(T^4 - T_\infty^4) \tag{27}$$

Here, T_∞ is the ambient temperature. Since there is a shielding gas flow over the surface, the convection heat loss cannot be omitted which is given by

$$q_{\text{conv}} = h_{\text{conv}}(T - T_\infty) \tag{28}$$

The boundary condition for the species equation on the top surface is given by

$$\frac{\partial f^\alpha}{\partial z} = 0 \tag{29}$$

2.3.3. Side surface (BC in Fig. 1)

$$-k\frac{\partial T}{\partial r} = q_{\text{conv}} \tag{30}$$

$$u = 0, \quad v = 0 \tag{31}$$

$$\frac{\partial f^\alpha}{\partial r} = 0 \tag{32}$$

2.3.4. Bottom surface (CD in Fig. 1)

$$-k\frac{\partial T}{\partial z} = q_{\text{conv}} \tag{33}$$

$$u = 0, \quad v = 0 \tag{34}$$

$$\frac{\partial f^\alpha}{\partial z} = 0 \tag{35}$$

2.3.5. Symmetrical axis (DE in Fig. 1)

$$\frac{\partial T}{\partial r} = 0 \tag{36}$$

$$u = 0, \quad \frac{\partial v}{\partial r} = 0 \tag{37}$$

$$\frac{\partial f^\alpha}{\partial r} = 0 \tag{38}$$

2.4. Plasma zone simulation

2.4.1. Governing equations

In current study, metal vapor in the keyhole is assumed to be a compressible, inviscid ideal gas. Since the heat production by viscous dissipation is rather small in laser welding, the energy equation can be simplified as [34]:

$$\frac{\partial}{\partial t}(\rho_{\mathrm{pl}}h_{\mathrm{pl}}) = \nabla\cdot\left(\frac{k_{\mathrm{pl}}}{c_{\mathrm{pl}}}\nabla h_{\mathrm{pl}} - \boldsymbol{q}_{\mathbf{r}}\right) + K_{\mathrm{pl}}I_{\mathrm{c}}(r) \times \exp\left(-\int_0^{z_{\mathrm{o}}} K_{\mathrm{pl}}\mathrm{d}z\right) + \sum_{m=1}^{n} K_{\mathrm{pl}}I_{r,m}(r,z) \times \exp\left(-\int_0^{z_m} K_{\mathrm{pl}}\mathrm{d}z\right) \tag{39}$$

where h_{pl} and ρ_{pl} represent, respectively, the enthalpy and density of the plasma, k_{pl} and c_{pl} represent, respectively, the thermal conductivity and specific heat of the plasma. $\boldsymbol{q}_{\mathrm{r}}$ stands for the radiation heat flux vector. Note $h_{\mathrm{pl}} = c_{\mathrm{pl}}T_{\mathrm{pl}}$.

The radiation source term $\nabla\cdot(\boldsymbol{q}_{\mathbf{r}})$ is defined as

$$\nabla\cdot\boldsymbol{q}_{\mathbf{r}} = k_{\mathrm{a}}\left(4\pi I_{\mathrm{b}} - \int_{4\pi} I\mathrm{d}\Omega\right) \tag{40}$$

where k_{a}, I_{b} and Ω denote the Planck mean absorption coefficient, blackbody emission intensity ($I_{\mathrm{b}} = \sigma T_{\mathrm{pl}}^4$) and solid angle, respectively. When an intense laser pulse interacts with the vapor in the keyhole, a significant amount of laser irradiation is absorbed by the ionized particles through the IB absorption. For simplicity, the plasma is assumed to be an absorbing–emitting medium and the scattering effect is neglected. The radiation transport equation (RTE) has to be solved for the total directional radiative intensity $I(\boldsymbol{r},\boldsymbol{s})$ [35]

$$(\boldsymbol{s}\cdot\nabla)I(\mathbf{r},\boldsymbol{s}) = k_{\mathrm{a}}(I_{\mathrm{b}} - I(\mathbf{r},\boldsymbol{s})) \tag{41}$$

where $\boldsymbol{s}$ and $\boldsymbol{r}$ denote a unit vector along the direction of the radiation intensity and the local position vector. When the plume within the keyhole is weakly ionized, the absorption mechanism mainly depends on electron-neutral interaction and the plume behaves as an optically thin medium. For the evaluation of the intensity and heat flux divergence, the Planck mean absorption coefficient is given as [35]

$$k_{\mathrm{a}} = \left(\frac{128}{27}k_{\mathrm{b}}\right)^{0.5}\left(\frac{\pi}{m_{\mathrm{e}}}\right)^{1.5}\frac{Z^2e^6\bar{g}}{h\sigma c^3}\frac{n_{\mathrm{e}}n_{\mathrm{i}}}{T_{\mathrm{pl}}^{3.5}} \tag{42}$$

2.4.2. Boundary conditions

2.4.2.1. Bottom surface inside the keyhole (EA in Fig. 1). Close to the liquid wall inside the keyhole, there is a so-called Knudsen layer where vaporization of material takes place. The vapor temperature across the Knudsen layer is discontinuous, which can be calculated by the following formula [28]:

$$\frac{T_{\mathrm{K}}}{T_{\mathrm{l}}} = \left[\sqrt{1+\pi\left(\frac{\gamma_{\mathrm{r}}-1}{\gamma_{\mathrm{r}}+1}\frac{m_{\mathrm{v}}}{2}\right)^2} - \sqrt{\pi}\frac{\gamma_{\mathrm{r}}-1}{\gamma_{\mathrm{r}}+1}\frac{m_{\mathrm{v}}}{2}\right]^2 \tag{43}$$

$$m_{\mathrm{v}}F = M_{\mathrm{K}}\sqrt{\frac{2}{\gamma_{\mathrm{r}}}} \tag{44}$$

where T_{K} is the vapor temperature outside of the Knudsen layer, T_{l} is the liquid surface temperature adjacent to the Knudsen layer, M_k is Mach number at the outer of the Knudsen layer and γ_{r} is the specific heat ratio. The value of m_{v} depends on the gas dynamics of the vapor flow away from the surface. $M_{\mathrm{K}} = 1.2$ is used in the present study [28]. The vapor is assumed to be iron in the form of monatomic gas with molecular weight of 56 and $\gamma_{\mathrm{r}} = 1.67$. The gas temperature outside the Knudsen layer is used as the boundary temperature. So the boundary condition is given by [35]:

$$T_{\mathrm{pl}} = T_{\mathrm{K}} \tag{45}$$

$$I = \varepsilon I_{\mathrm{b}} + \frac{1-\varepsilon}{\pi}\int_{\vec{n}\cdot\Omega'<0} I|\vec{n}\cdot\Omega|\mathrm{d}\Omega' \tag{46}$$

2.4.2.2. Top surface outside the keyhole (FA in Fig. 1).

$$T_{\mathrm{pl}} = T_{\infty} \tag{47}$$

$$I = I_{\mathrm{c}}(r) \tag{48}$$

2.4.2.3. Symmetrical axis (EF in Fig. 1).

$$\frac{\partial T_{\mathrm{pl}}}{\partial r} = 0 \tag{49}$$

$$\frac{\partial I}{\partial r} = 0 \tag{50}$$

3. Numerical method

The solutions of transport equations in the metal zone and in the plasma zone are coupled; that is, the simulations of the metal and the plasma zone provide boundary conditions for each other. However, there are large spatial and physical differences between the metal and the plasma zone. To enhance convergence rate and save calculation time, different time and space resolutions are used for the metal and the plasma zone. The governing equations (Eqs. (1)–(5) and Eq. (39)) and all related supplemental equations and boundary conditions are solved through the following iterative scheme:

1. Eqs. (1)–(4) are solved iteratively for the metal zone to obtain velocity, pressure and temperature distributions using the associated boundary conditions.
2. Eq. (5) is solved for the metal zone to obtain concentration distributions using the associated boundary conditions.
3. Eq. (39) is solved iteratively to obtain the plasma temperature distributions in the keyhole under the associated boundary conditions. The steps for solving Eq. (39) are listed below:

(a) Solve Eq. (41) using the associated boundary conditions to get the total directional radiative intensity distributions.
(b) Solve Eq. (40) to get radiation source term $\nabla \cdot (\boldsymbol{q}_r)$.
(c) Solve Eqs. (23) and (22) in the order using the most recent plasma temperature from the previous time step to get the updated plasma absorption coefficient K_{pl}.
(d) Solve Eq. (39) to get the updated plasma temperature.

4. Solve VOF algorithm Eq. (6) to obtain the new domain for the metal and plasma zones.
5. Update boundary conditions for the metal and the plasma zones.
6. Advance to the next time step and back to Step 1 until the desired time is reached.

The techniques for solving Eqs. (1)–(5) and Eq. (39) are given by Wang and Tsai [25]. Following the MAC scheme, the r- and z-velocity components are located at cell face centers on lines of constants r and z respectively; while the pressure, VOF function, temperature and absorbed laser flux are located at cell centers. Since the temperature and pressure field change more dramatically near the keyhole, a non-uniform grid system with 202×252 points is used for the total computational domain of 5.0 mm $\times$ 20.0 mm, in which smaller grids are concentrated near the keyhole and larger grids for other parts. Due to the axis-symmetry of the domain, only half of the grid points were used in the calculation. Calculations were executed on the DELL OPTIPLEX GX270 workstations with LINUX-REDHAT 9.0 OS and it took about 6.5 h of CPU time to simulate about 100 ms of real-time welding. The average time step is 10^{-4} s and the smallest time step is about 10^{-6} s.

4. Results and discussion

The base metal is assumed to be 304 stainless steel containing 100 ppm sulfur. The process parameters and thermophysical properties used in the present study are summarized in Table 1. The laser energy is assumed to be in the Gaussian distribution and the focus plane is on the top surface of the base metal. In this study, MIG droplets are assumed to be steadily generated via a certain wire feeding method right after the shut-off of the laser. The droplet is made of 304 stainless steel containing 300 ppm sulfur and its size, initial temperature, velocity, and generation frequency are all given in the calculation. Arc heat and arc pressure are used as constants in the current study. In the future, electrode melting, droplet generation, arc plasma generation [36] will be integrated into current models. Note, in this study, the element 'sulfur' is used just as a media to trace the mixing process in the weld pool. In this sense, it will not affect the mixing process in the weld pool.

Table 1
Thermophysical properties of 304 stainless steel and process parameters

Nomenclature	Value
Constant in Eq. (12), A (Pa)	1.78×10^{10}
Constant in Eq. (16), A_v	2.52
Vaporization constant in Eq. (11), B_0	0.55
Speed of light, c (m s^{-1})	3×10^8
Specific heat of solid phase, c_s (J kg^{-1} K^{-1})	700
Specific heat of liquid phase, c_l (J kg^{-1} K^{-1})	780
Specific heat of plasma, c_{pl} (J kg^{-1} K^{-1})	900
Charge of electron, e (C)	1.6022×10^{-19}
Ionization potential for neutral atoms, E_i (J)	1.265×10^{-18}
Sulfur concentration in base metal, f^{∞} (ppm)	100
Gravitational acceleration, g (m s^{-2})	9.8
Degeneracy factors for electrons, g_e	30
Degeneracy factors for ions, g_i	30
Degeneracy factors for neutral atoms, g_0	25
Quantum mechanical Gaunt factor, $\bar{g}$	1.5
Convective heat transfer coefficient, h_{conv} (W m^{-2} K^{-1})	80
Planck's constant, $\bar{h}$ (J s)	6.625×10^{-34}
Latent heat of fusion, H (J kg^{-1})	2.47×10^5
Thickness of substrate metal, H_b (mm)	3.0
Latent heat of vaporization, H_v (J kg^{-1})	6.34×10^6
Boltzmann's constant, k_b (J K^{-1})	1.38×10^{-23}
Thermal conductivity of liquid phase, k_l (W m^{-1} K^{-1})	22
thermal conductivity of plasma, k_{pl} (W m^{-1} K^{-1})	3.74
Thermal conductivity of solid phase, k_s(W m^{-1} K^{-1})	22
Atomic mass, m_a (g)	9.3×10^{-23}
Electron mass, m_e (g)	9.1×10^{-28}
Mach number at the outer of the Knudsen layer, M_K	1.2
Avogadro's number, N_a (mol^{-1})	6.022×10^{23}
Laser power, P_{laser} (W)	1700
Laser beam radius, r_f (mm)	0.2
Laser beam radius at focus, r_{f0} (mm)	0.2
Laser pulse duration t_p (ms)	15
Gas constant, R (J kg^{-1} mol^{-1})	8.3×10^3
Radius of substrate metal, R_b (mm)	20.0
Liquidus temperature, T_l (K)	1727
Reference temperature, T_0 (K)	2500
Solidus temperature, T_s (K)	1670
Ambient temperature, T_∞ (K)	300
Average ionic charge in the plasma, Z	1
Thermal expansion coefficient, β_T (K^{-1})	4.95×10^{-5}
Surface radiation emissivity, ε	0.4
Dielectric constant, ε_0	14.2
Constant in Eq. (18), ε_f	0.2
Specific heat ratio, γ_r	1.6
Angular frequency of laser radiation, ω (rad s^{-1})	1.78×10^{14}
Dynamic viscosity, μ_l (kg m^{-1} s^{-1})	0.006
Stefan–Boltzmann constant, σ (W m^{-2} K^{-4})	5.67×10^{-8}
Electrical conductivity, σ_e (Ω^{-1} m^{-1})	7.14×10^{-5}
Density of liquid phase, ρ_l (kg m^{-3})	6900
Density of plasma, ρ_{pl} (kg m^{-3})	0.06
Density of solid phase, ρ_s (kg m^{-3})	7200

4.1. Interaction between MIG droplets and weld pool

Fig. 2 shows the process of droplet-weld pool interaction and keyhole collapse in hybrid laser-MIG welding. The corresponding distributions of temperature, sulfur concentration, and melt flow velocity are given in Figs. 3–5, respectively. Since only the interaction between filler droplets and weld pool is of primary concern in this study, the keyhole formation process, which is similar to what was

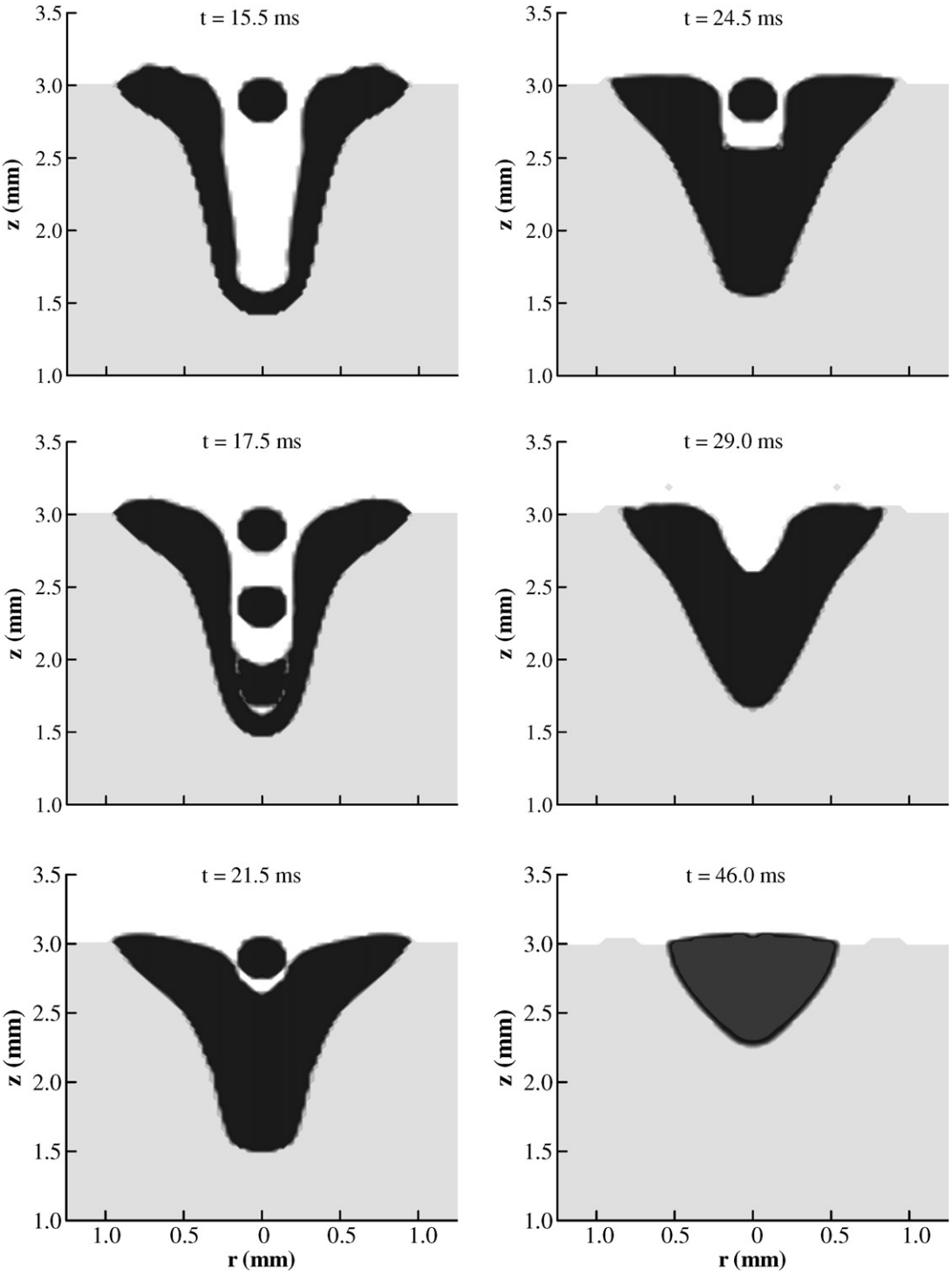

Fig. 2. A sequence of metal evolution showing the impingement process of filler metal into the weld pool in hybrid laser-MIG welding.

previously discussed [20], is ignored. As shown in Fig. 2, filler droplets start to fall into the keyhole at $t = 15.0$ ms. The diameter of a typical filler droplet is assumed to be 0.35 mm, at an initial speed of 0.5 m/s, initial temperature 2400 K, and frequency 1000 Hz (i.e., a droplet per 1 ms). As shown in Fig. 3, since the laser had been turned off at this time, the temperature of the keyhole wall drops very quickly, especially in the lower part of the keyhole due to the existence of only a thin layer of liquid metal. Once the laser is turned off and the temperature drops, the laser-induced recoil pressure sustaining the keyhole quickly decreases. Under the actions of surface tension and hydrostatic pressure, the molten metal near the keyhole shoulder has a tendency to flow back to refill the keyhole and the size of the keyhole is reduced. In the process of falling into the keyhole, filler droplets are continuously accelerated by gravity and arc pressure, although the acceleration effect is weakened by the air resistance, as shown in Fig. 5. When the first droplet

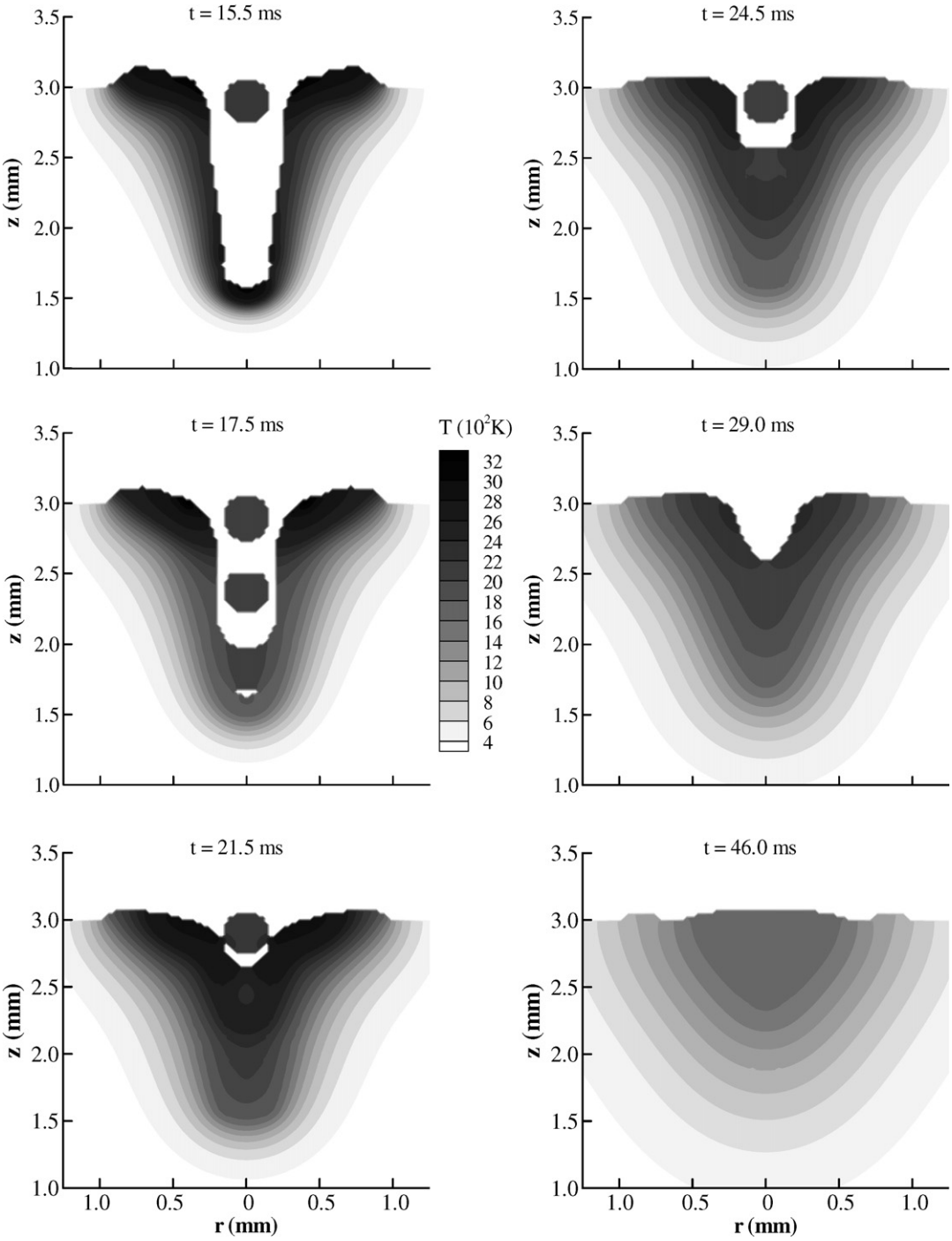

Fig. 3. The corresponding temperature distributions as shown in Fig. 2.

impinges into the weld pool at $t = 17.5$ ms, the downward momentum carried by the droplet forces it to flow downward and outward along the keyhole wall. This can be clearly found in Fig. 4 by tracing the sulfur concentration distributions. Meanwhile, the downward momentum from the droplet squeezes the molten metal in the weld pool casing it to flow upward and outward. However, under the actions of hydrostatic force and surface tension, the molten metal on the keyhole wall has a tendency to flow downward along the keyhole wall. So the upward flowing melt caused by the push of the droplet impingement will be mitigated, which makes it difficult for the droplet liquid to further flow downward. As shown in Fig. 2 at $t = 21.5$ ms, when the subsequent droplets continue to impinge into the keyhole, the molten metal level in the center of the weld pool rises instead of falling.

As shown in Fig. 4, for the first several droplets, the filler metal mainly diffuses along the longitudinal direction and only the first droplet can spread out in the latitudinal direction along the solid–liquid interface driven by the

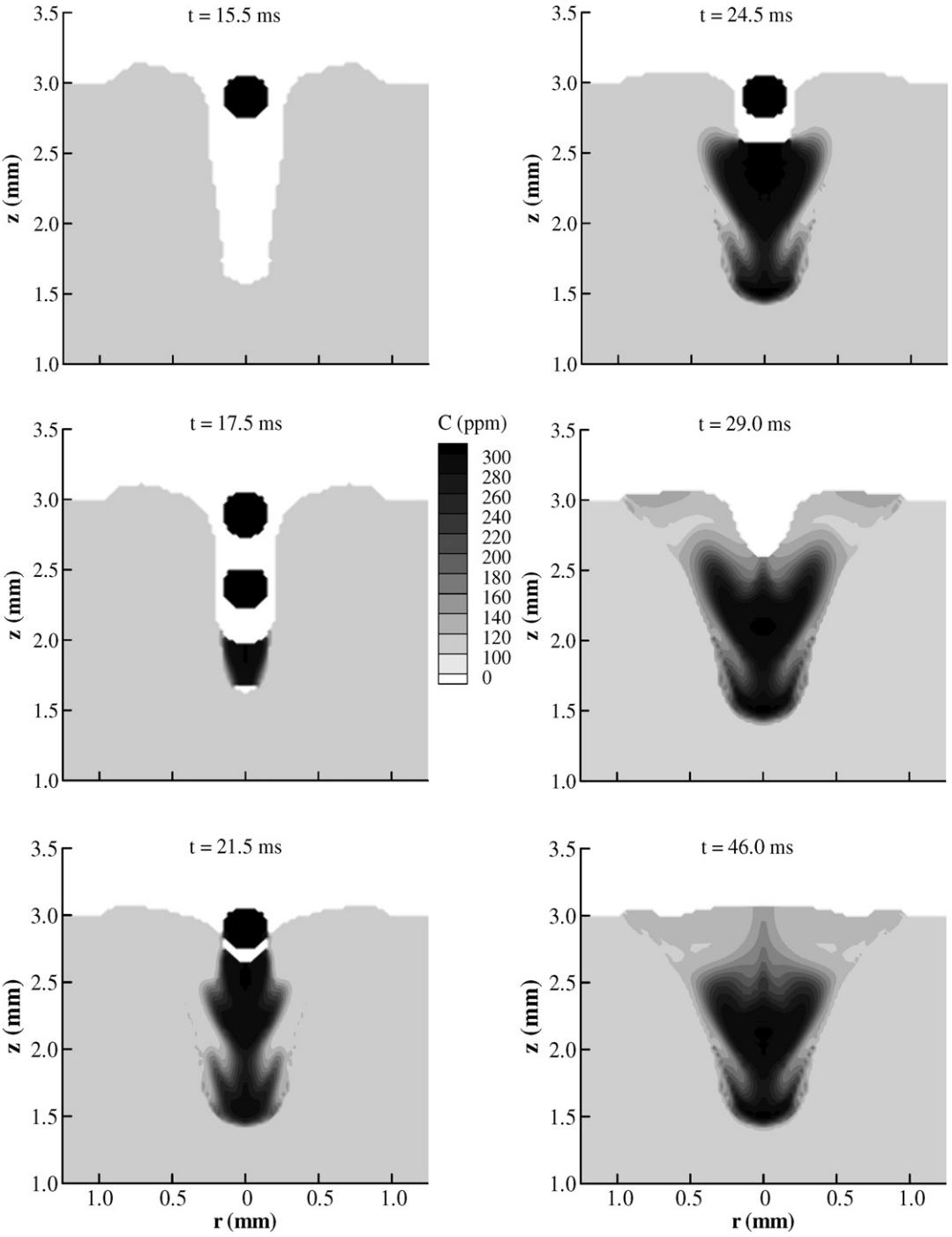

Fig. 4. The corresponding sulfur concentration distributions as shown in Fig. 2.

downward momentum. However, as more and more droplets impinge into the weld pool, as shown in Fig. 5 at $t = 21.5$ ms, an anti-clockwise vortex is found in the middle of the keyhole. The formation of the vortex helps the filler metal to diffuse outward along the latitudinal direction, as shown in Fig. 4. The formation and size of the vortex depend on the interaction among the droplets and the weld pool in the impinging process. As discussed before, when the laser is turned off, under the actions of hydraulic force and surface tension, the molten metal on the shoulder will flow downward along the keyhole wall from the top. Meanwhile, since the molten metal is incompressible, the strong downward flow in the center of the weld pool, caused by the impingement of the droplet, pushes some molten metal causing it to flow upward. The kinetic energy of the melt flow in the center is transferred into the potential and kinetic energy of the outward flowing melt. So the downward momentum of the flow in that region becomes smaller and smaller. Finally the melt flow changes its direction from flowing downward to flow outward along the solid–liquid interface, as shown in Fig. 5 at $t = 21.5$ ms. When the molten metal flows upward along the solid–liquid inter-

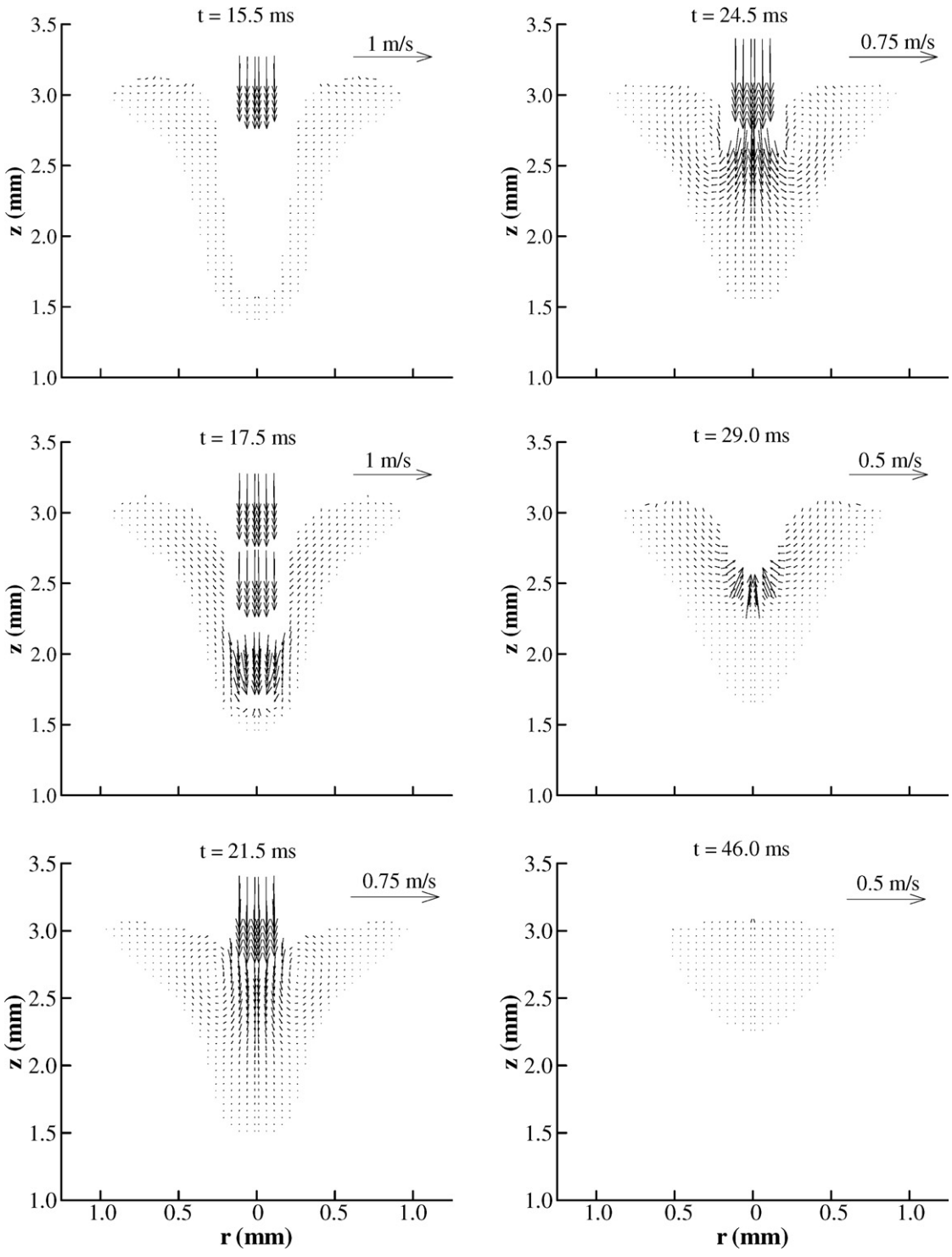

Fig. 5. The corresponding velocity distributions as shown in Fig. 2.

face, the kinetic energy of the melt flow is transferred into potential energy and the upward velocity becomes smaller and smaller. Finally the melt flow changes its direction to flow inward when it meets the back-filling melt flow from the shoulder of the keyhole. Hence, a vortex is formed in the middle of the keyhole. As the filler droplets continue to impinge into the weld pool, more and more downward momentum is added into the center of the weld pool, the vortex affected zone is enlarged and the strength of the vortex is enhanced. This vortex flow helps the filler metal to diffuse along the latitudinal direction. As shown in Fig. 4, at $t = 24.5$ ms, the diffusion zone of the filler metal is much larger than that at $t = 21.5$ ms. Since the latitudinal diffusion of filler metal has a close relationship with the vortex, the evolution of the vortex can be estimated by tracing the shape of the diffusion zone in the final fusion zone. Also, as

noticed at $t = 24.5$ ms, the downward velocity of the liquid metal in the center of the weld pool is quite large and the mass from droplets is not enough to compensate the downward mass flow in that area. Hence, the liquid surface level is found to be lower in the center of the weld pool.

After $t = 25.0$ ms, no droplet is added into the weld pool. The melt flow near the center of the keyhole is bouncing back under the actions of hydrostatic force and surface tension. As shown at $t = 29.0$ ms in Fig. 6, the melt flow starts to flow inward and downward and the size of the keyhole is becoming smaller and smaller. Finally the keyhole is completely filled back, as shown at $t = 49.0$ ms in Fig. 2. During the back-filling process, the vortex flow becomes weaker and weaker. So the diffusion of filler metal in the latitudinal direction is not improved much at this stage. This can be found by comparing the figures at $t = 29.0$ ms and at $t = 46.0$ ms in Fig. 4. Also, as shown at $t = 46.0$ ms in Fig. 4, only a small amount of the filler metal, which is brought there by the bouncing flow, is found near the center of the weld pool. Hence, it can be concluded that most of the back-filling liquid metal comes from the upper shoulder of the keyhole instead of from filler droplets.

As shown in Fig. 4, the supplemental heat brought into the weld pool by the droplets and the arc helps to delay the solidification process. The delayed solidification process gives more time for the filler droplets to diffuse into the base metal. After the termination of droplet generation, the heat input carried by the droplets also ceases. Due to the rapid heat loss to the base metal by conduction and to the surroundings by radiation and convection, the size of the molten pool quickly becomes smaller and smaller when the solidification proceeds. At $t = 46.0$ ms, the melt flow in the weld pool is almost diminished and the temperature distribution becomes more uniform than before, as shown in Figs. 4 and 6. After that, the shape and the composition of the weld pool change very little as compared to those in the final weld.

4.2. Modification of composition by adding filler droplets

As discussed above, the crack resistance of the hybrid laser-MIG weld can be improved by adding anti-crack elements into the base metal via filler droplets. However, the solidification process proceeds very fast due to the small weld pool size and fast cooling rate in hybrid laser-MIG welding. Hence, the time available for the filler metal to diffuse into the base metal is very short in hybrid laser-MIG welding compared with that in a conventional arc welding process. Good diffusion of filler metal into the weld pool is very difficult if the welding parameters are not controlled in a proper way. As shown in the above studies of hybrid laser-MIG welding, how well filler droplets can diffuse into the weld pool is found to be dependent on the competition between the rate of mixing and the rate of solidification. Then, we further study the effect of the droplet size on the diffusion process, as shown in Fig. 6. In this study, for a typical droplet, the initial velocity is 0.5 m/s, the generation frequency is 1000 HZ and the droplet feeding starts at $t = 15$ ms and terminates at $t = 25$ ms. In hybrid laser-MIG welding, the size of the droplet mainly depends on the diameter of the feeding wire. In order to analyze the effect of droplet size on the mixing and diffusion processes, three simulations are carried out with the droplet size at 0.3 mm, 0.35 mm, and 0.4 mm, respectively.

As shown in Fig. 6, with the increase of the diameter of the droplet, the latitudinal diffusion of filler metal into the weld pool is improved. According to our previous analysis of the mixing process, the latitudinal diffusion of the filler metal into the weld pool is found to be closely associated with the formation of the vortex in the weld pool. The strength and the size of the vortex depend on the downward momentum of the filler droplets, which is the product of droplet mass and velocity. As the droplet size increases, the downward momentum increases, which leads to a stronger and larger vortex. So the diffusion zone is enlarged outward, especially in the middle of the keyhole where the vortex is located. This can be found by comparing the figures for $d = 0.30$ mm and $d = 0.35$ mm in Fig. 6. Meanwhile, stronger downward momentum from a larger droplet also leads to a strong bouncing flow near the center of the keyhole after termination of droplet feeding, which helps the filler metal to diffuse into the upper part of the final weld, as shown in Fig. 6 for $d = 0.40$ mm. Moreover, larger droplet size brings more

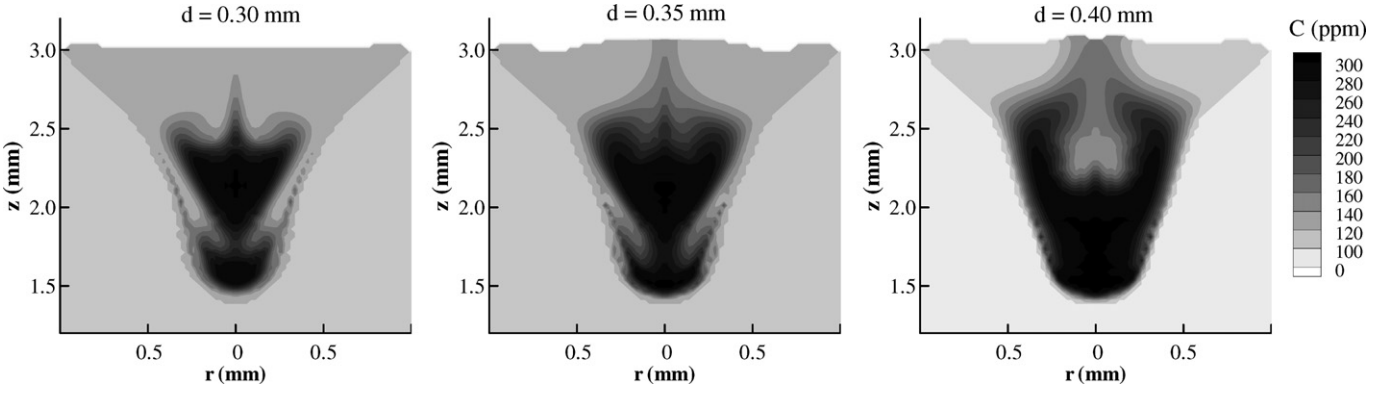

Fig. 6. Effect of droplet size on the sulfur distribution in the weld.

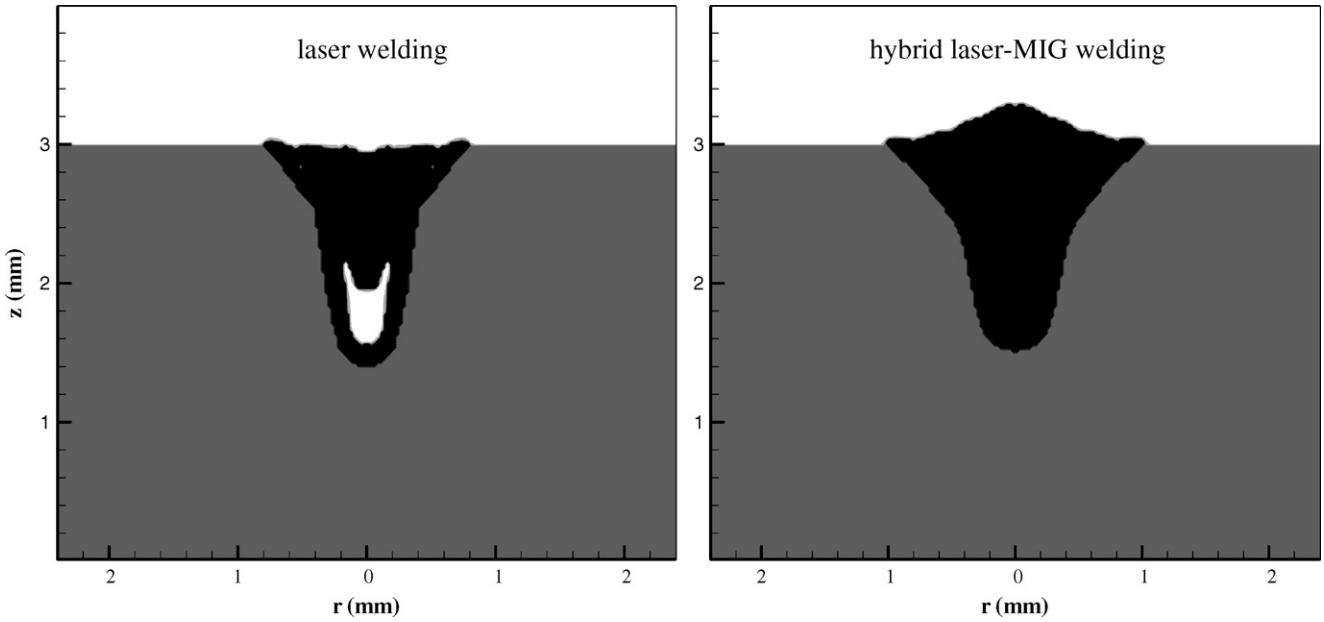

Fig. 7. The comparison of the weld bead geometry between a laser weld and a hybrid laser-MIG weld.

heat input into the weld pool. It helps to delay the solidification of the fusion zone. The delayed solidification process gives more time for the filler metal to mix and diffuse into the weld pool. However, larger droplets also bring some negative effects on the diffusion of filler metal near the center of the weld zone. After the termination of the droplet feeding, the level of the fluid surface near the center of the weld pool continues to go down due to the larger hydrodynamic pressure caused by the downward momentum. This leads to a deep hole in the center of the weld pool where the impinging process occurs. During the back-filling process of this hole, some metal from the upper part of the keyhole flows into the bottom of this hole. Since the concentration of filler metal in the upper part of the keyhole is very low, it causes a low diffusion zone of filler metal in the center of the final weld, as shown in Fig. 6 for $d = 0.40$ mm.

4.3. Porosity elimination and weld profile modification

Fig. 7 shows the comparison of the cross-sectional area between a typical hybrid laser-MIG weld and a typical laser weld. Some undercuts are clearly found in the laser weld. In laser welding some base metal is lost due to evaporation. Meanwhile, during the keyhole collapse process, the liquid–solid interface moves inward and upward very quickly because of strong heat dissipation to the surrounding metal. Some liquid metal has no time to flow back to its original position before its complete solidification, especially for the liquid metal at the upper part of the cold edge. Hence, an undercut is found near the edge of the top surface of the final weld bead, as shown in Fig. 7. This is one of the major defects for laser welds. Also, in laser welding, a pore/void is found in the final weld. Detailed discussion on the formation of porosity in laser welding can be found in Ref. [20] and will not be repeated here.

In hybrid laser-MIG welding, since there are some droplets impinging into the weld pool when the laser is turned off, the addition of metal from the droplets into the weld pool can help to eliminate pore/void formation and compensate the mass loss. The momentum and energy carried by droplets also affect the melt flow and the heat transfer in the weld pool, and thus the shape of the final weld. The total effect is dependent on the characteristics of the filler droplets. In the current study, for a typical filler droplet, the diameter is 0.35 mm; the initial speed is 0.25 m/s; initial temperature is 2400 K; generation frequency is 1000 Hz; duration is 25 ms and the rest of the welding conditions are the same as before. As shown in Fig. 7, the final weld bead shape is improved in hybrid laser-MIG welding. There is no porosity and undercut found in the final weld and the topology of the weld bead is better than that of the laser weld due to the additional metal input from the droplets. The supplemental heat input from the arc is transferred to the weld pool mainly in the region near the top of the weld pool, which makes the top portion of the hybrid weld wider than that of the laser weld. In addition, in the current study, the penetration depth in hybrid laser-MIG welding is found to be almost the same as that in laser welding. It indicates that the penetration depth in hybrid laser-MIG welding mainly depends on the laser power, rather than the arc power.

5. Conclusions

Mathematical models have been developed to investigate the transport phenomena in a hybrid laser-MIG welding process. The complicated velocity and temperature

distributions caused by the impingement of filler droplets are calculated. The mixing between base metal and MIG droplets in the fusion zone is traced by the concentration of sulfur.

As shown in the study, the mixing and diffusion of the filler droplets into the base metal is greatly affected by the dynamics of the weld pool fluid flow. The competition between the rate of mixing and the rate of solidification determines the compositional homogeneity of the weld pool. The welding parameter, such as filler droplet size (wire diameter) can influence the rate of mixing and/or the rate of solidification. Increasing the droplet size can enhance the vortex formation in the weld pool created by the downward momentum carried by the droplets. It can improve the latitudinal diffusion of the filler droplet in the fusion zone. However, too large of a droplet will leave a low diffusion zone of filler metal at the center of the final weld. Also, by adding of additional metal into the weld pool via the MIG droplets in hybrid laser-MIG welding, the final weld bead shape can be modified. Porosity and undercuts can be eliminated. The developed model can be used for further parametric studies or optimization of the hybrid laser-MIG welding process.

Acknowledgements

It is gratefully acknowledged that this research is partially supported by the General Motors Corporation. Also, special thanks go to Professor Terry F. Lehnhoff for beneficial discussions with him.

References

[1] W. Duley, Laser Welding, John Wiley & Sons Inc., 1999.
[2] C. Dawnes, Laser Welding, McGraw-Hill Inc., 1992.
[3] C. Schinzel, B. Hohenberger, F. Dausinger, H. Hügel, Laser welding of aluminum car bodies – from research to production, Proc. ICALEO Sec. F (1998) 56–65.
[4] T. Ishide, S. Tsubota, M. Nayama, Y. Shimokusu, T. Nagashima, K. Okimura, 10 kW class YAG laser application for heavy components, SPIE High-Power Lasers Manuf. 3888 (1999) 543–550.
[5] L.P. Connor, Welding Handbook, eighth ed., American Welding Society, 1987.
[6] J.E. Hatch, Aluminum: Properties and Physical Metallurgy, American Society for Metals, Metals, 1984.
[7] J.H. Dudas, F.R. Collins, Preventing weld cracks in high-strength aluminum alloys, Weld. J. 45 (1966) 241s–249s.
[8] M.J. Cieslak, P.W. Fuerschbach, On the weldability, composition, and hardness of pulsed and continuous Nd: YAG laser welds in aluminum alloys 6061, 5456, and 5086, Metall. Trans. 19B (1988) 319–329.
[9] M. Ono, Y. Shinbo, A. Yoshitake, M. Ohmura, Development of laser-arc hybrid-welding, NKK Techn. Rev. 86 (2002) 8–12.
[10] A. Weisheit, R. Galun, B.L. Mordike, CO_2 laser beam welding of magnesium-based alloys, Weld. J. 77 (4) (1998) 149s–154s.
[11] M. Kutsuna, L. Chen, Interaction of both plasmas in CO_2 laser – MAG hybrid welding of carbon steel, Proc. SPIE 4831 (2002) 341–346.
[12] T. Ishide, S. Tsubota, M. Watanabe, Latest MIG TIG arc-YAG laser hybrid welding systems for various welding products, Proc. SPIE 4831 (2002) 347.
[13] H. Staufer, M. Rührnößl, G. Miessbacher, Hybrid welding for the automotive industry, Ind. Laser Solut. 7 (2003).
[14] H. Engström, K. Nilsson, J. Flinkfeldt, T. Nilsson, A. Skirfors, B. Gustavsson, Laser hybrid welding of high strength steels, Proc. ICALEO 2001 (2001) 125–134.
[15] S. Missouri, A. Sili, Structural characterization of C–Mn steel laser beam welded joints with powder filler metal, Weld. J. 79 (11) (2000) 317–323.
[16] J.R. Hwang, J.L. Doong, C.C. Chen, Fatigue crack growth in laser weldments of a cold rolled steel, Mater. Trans. J. 37 (8) (1996) 1443–1446.
[17] E. Schubert, M. Klassen, J. Skupin, G. Sepold, Int. Conf. Weld. Melt. Electron Laser Beam (1998) 195.
[18] Y. Naito, S. Katayama, A. Matsunawa, Keyhole behavior and liquid flow in molten pool during laser-arc hybrid welding, Proc. SPIE 4831 (2002) 357–362.
[19] S. Sun, T. Moisio, Laser beam welding of austenitic/ferritic dissimilar steel joints using nickel based filler wire, Mater. Sci. Technol. (1993) 603–608.
[20] J. Zhou, H.L. Tsai, P.C. Wang, Transport phenomena and keyhole dynamics during pulsed laser welding, ASME J. Heat Transfer 128 (2006) 680–690.
[21] D.B. Kothe, R.C. Mjolsness, M.D. Torrey, Ripple: A Computer Program for Incompressible Flows with Free Surfaces, LA-12007-MS, Los Alamos National Laboratory, 1991.
[22] K.C. Chiang, H.L. Tsai, Shrinkage-induced fluid flow and domain change in two-dimensional alloy solidification, Int. J. Heat Mass Transfer 35 (1992) 1763–1769.
[23] I. Miyamoto, E. Ohmura, T. Maede, Dynamic behavior of plume and keyhole in CO_2 laser welding, Proc. ICALEO Sec. G (1997) 210–218.
[24] J. Dowden, N. Postacioglu, M. Davis, P. Kapadia, A keyhole model in penetration welding with a laser, J. Phys. D: Appl. Phys. 20 (1987) 36–44.
[25] Y. Wang, H.L. Tsai, Impingement of filler droplets and weld pool dynamics during gas metal arc welding process, Int. J. Heat Mass Transfer 44 (2001) 2067–2080.
[26] P. Sahoo, T. DeBroy, M.J. Mcnallan, Surface tension of binary metal-surface active solute systems under conditions relevant to welding metallurgy, Metall. Trans. 19B (1988) 483–491.
[27] R.T.C. Choo, J. Szekely, S.A. David, On the calculation of the free surface temperature of gas–tungsten-arc weld pools from first principles: part II. Modeling the weld pool and comparison with experiments, Metall. Trans. 23B (1992) 371–384.
[28] C.J. Knight, Theoretical modeling of rapid surface vaporization with back pressure, AIAA J. 17 (1979) 519–523.
[29] V. Semak, A. Matsunawa, The role of recoil pressure in energy balance during laser materials processing, J. Phys. D: Appl. Phys. 30 (1997) 2541–2552.
[30] T. Zacharia, S.A. David, J.M. Vitek, Effects of evaporation and temperature-dependent material properties on weld pool development, Metall. Trans. 22B (1991) 233–241.
[31] Yu.P. Raizer, Laser-Induced Discharge Phenomena, Consultants Bureau, New York, 1977.
[32] L. Spitzer, Physics of Fully Ionized Gases, Interscience Publishers, New York, 1967.
[33] H. Kogelnik, T. Li, Laser beams and resonators, Appl. Opt. 5 (10) (1966) 1550–1554.
[34] R. Siegel, J.R. Howell, Thermal Radiation Heat Transfer, third ed., Hemisphere Publishing Corporation, 1992 (Chapter 13).
[35] R. Ho, C.P. Grigoropoulos, J.A.C. Humphrey, Gas dynamics and radiation heat transfer in the vapor plume produced by pulsed laser irradiation of aluminum, J. Appl. Phys. 79 (1996) 7205–7215.
[36] F.L. Zhu, H.L. Tsai, S.P. Marin, P.C. Wang, A comprehensive model on the transport phenomena during gas metal arc welding process, Progr. Comput. Fluid Dyn. 4 (2) (2004) 99–117.